

Check for updates







The Importance of the Design of Porous Transport Layers: Unveiling the Interplay Between Structure, Mechanics, and Electrochemistry in Anion Exchange **Membrane Water Electrolysis**

Jagoda Justyna Manss-Chmielarz¹ D | Tobias Morawietz¹ | Karl Iddon² | Steffen Rehse³ D | Aldo Saul Gago¹ D | Kaspar Andreas Friedrich^{1,4}

¹Institute of Technical Thermodynamics, Electrochemical Energy Technology, German Aerospace Center (DLR), Stuttgart, Baden-Württemberg, Germany | 2Knitmesh Technologies Ltd, Greenfield, Flintshire, UK | 3Institute of Technical Thermodynamics, Electrochemical Energy Technology, German Aerospace Center (DLR), Oldenburg, NS, Germany | 4 Institute for Building Energetics, Thermotechnology and Energy Storage, University of Stuttgart, Stuttgart, Baden-Württemberg, Germany

Correspondence: Aldo Saul Gago (aldo.gago@dlr.de)

Received: 28 January 2025 | Revised: 14 May 2025 | Accepted: 17 June 2025

Funding: The study was supported by the European Union and the Clean Hydrogen Joint Undertaking (Grant no. 101112055).

Keywords: anion exchange membrane water electrolysis | anode | design | mesh | porous transport layers

ABSTRACT

The global drive for sustainable energy solutions intensified interest in anion exchange membrane water electrolysis (AEMWE), as a promising hydrogen production pathway, leveraging renewable energy sources. However, widespread adoption is hindered by the high cost and non-optimised design of crucial components, such as porous transport layers (PTL) and flow fields. This study comprehensively investigates the interplay between structure, mechanics, and electrochemical performance of a low-cost knitted wire mesh PTL, focusing on its potential to enhance cell assembly and operation. Electrochemical characterisation was performed on a single 4 cm² cell, using 1 M KOH at 60°C. Knitted wire mesh PTL, characterised by approximately 70% porosity. 2 mm thickness, and 1.098 tortuosity, delivered a 33% improvement in current density compared to the standard cell configuration. Introducing a knitted PTL interlayer reduced cell voltage by 74 mV at 2 A cm⁻² by improving compression force distribution across the active area, enhancing gas transport and maintaining optimal electrical and thermal conductivity. These findings highlight the significant potential of innovative PTL designs in AEMWE to improve mechanical and operational efficiency without increasing the cost.

1 | Introduction

Anion exchange membrane water electrolysis (AEMWE) is a rapidly expanding branch of low-temperature polymer electrolyte membrane electrolysers for green hydrogen production. It is gaining traction as an alternative technology to alkaline water electrolysis (AWE) and proton exchange membrane water electrolysis (PEMWE). Similar to AWE, AEMWE operates in an

alkaline environment and can be employed with non-noble electrode materials. While AWE uses a thick ceramic diaphragm as the gas separator, the membrane in AEMWE technology allows for reduced ohmic resistance of the cell. Moreover, AEMWE operates in a less alkaline environment than AWE, with a future aim to operate with the pure water electrolyte [1]. In contrast to alkaline environment electrolysis, PEMWE has so far demonstrated the highest performance;

This is an open access article under the terms of the Creative Commons Attribution License, which permits use, distribution and reproduction in any medium, provided the original work is properly

© 2025 The Author(s). Carbon Energy published by Wenzhou University and John Wiley & Sons Australia, Ltd.

however, this comes at a high material cost due to the use of iridium (Ir) and platinum (Pt) as common catalysts, as well as titanium (Ti) or Pt-coated Ti for structural components required to withstand its highly acidic environment [2]. Additionally, the proton-conducting function is enabled by the commercially employed Nafion membrane, based on the perfluorinated sulphonic acid (PFSA) ionomer. This component encompasses a particular set of drawbacks not only due to its cost and thermochemical stability, but most importantly due to its environmental and health hazard, including the Nafion byproducts (polyfluoroalkyl ether sulphonic acid) [3, 4]. The proposed PFAS bans in several countries could be a serious setback to PEMWE technologies, making it even more important to develop alternatives. Considering the technological constraints of AWE and limitations stemming from environmental concerns associated with PEMWE, AEMWE stands for an efficient, cost-effective, and environmentally sustainable alternative in the electrolysis field.

Employing a zero-gap configuration (detailed in Figure 1A), AEMWE relies strongly on efficient gas removal from the electrode so that the evolved gas bubbles do not dwell on the catalyst area blocking the active reaction sites. Furthermore, the membrane electrode assembly (MEA) requires good electrical contact

and two-phase flow properties on one hand alleviating reaction kinetics at the three-phase interface and on the other reducing interfacial contact resistance (ICR) between the layers, both having a great impact on efficiency [5]. Hence, a porous transport layer (PTL) is a significant component in the upscaling considerations of the electrolysis technology. It provides crucial mechanical stability under the cell compression, distributing the clamping force. It ensures electrical contact to the catalyst layer and facilitates the two-phase flow allowing the electrolyte to reach the membrane against the flow of produced gases. Therefore, when poorly designed, the PTL can exacerbate mass transport problems through slow electrolyte flow in hightortuosity structures or hinder bubble detachment at the MEA interface. A poorly optimised PTL can also be the cause of heterogeneous compression distribution, leading to heterogeneous current density distribution and poor electrocatalyst utilisation. In severe cases, localised force maxima could lead to premature membrane punctures [6].

Recent advancements in PTL design have focused on addressing these limitations through novel materials and structural innovations. Among the most widely studied PTLs are sintered metal fibre felts, particularly those made from Ti for PEMWE, stainless steel (ss), and, to a lesser extent, nickel (Ni) for

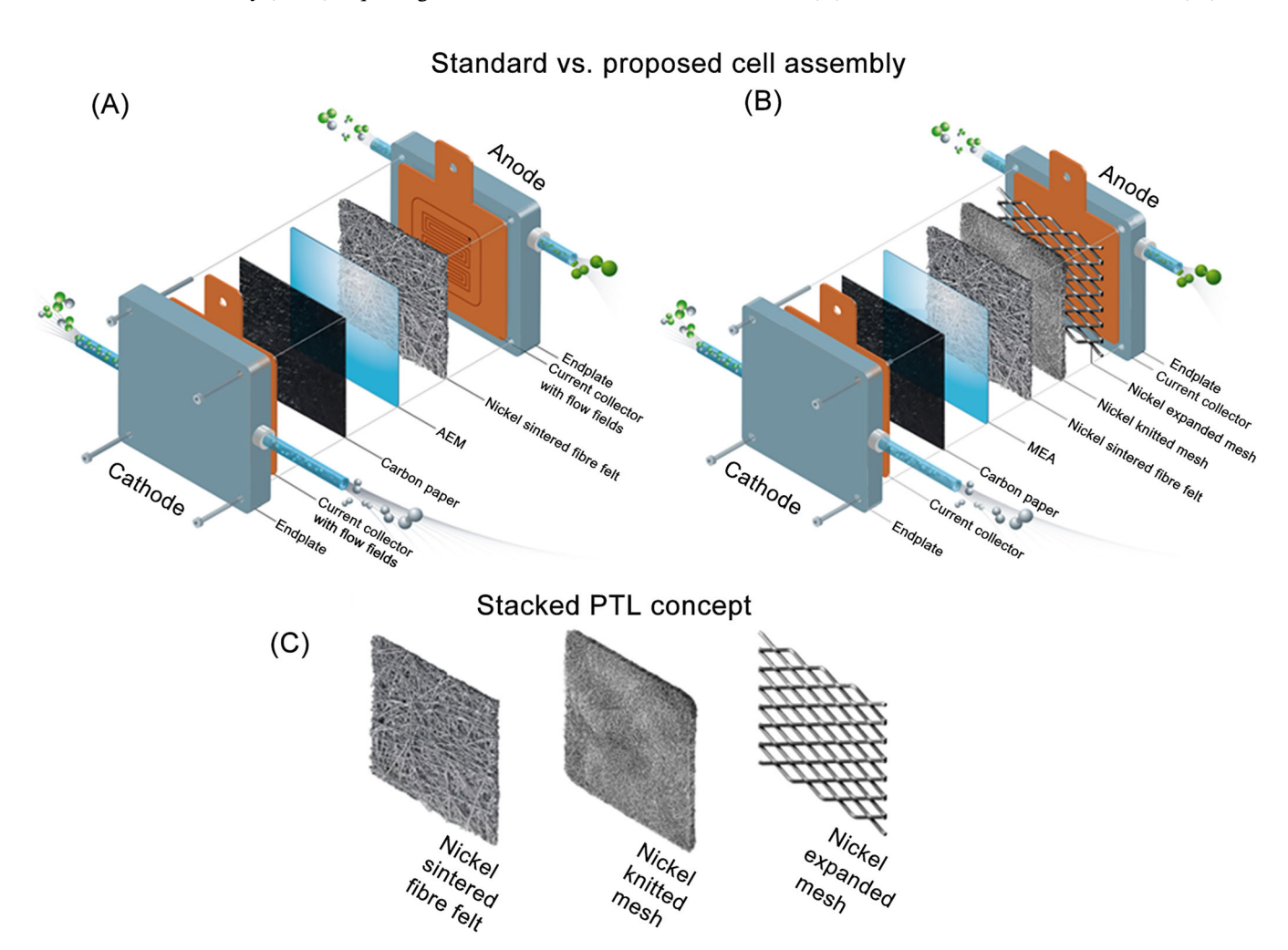


FIGURE 1 | (A) Visual representation of the conventional cell assembly including component-current collectors with flow fields, selected PTLs and AEM. (B) Proposed novel structure comprising of bipolar membrane (BPP) without flow field, and 'stacked-PTL' anode concept including EXM, KM, and felt. (C) Components of the proposed anode PTL concept in this study.

AEMWE. These materials offer excellent tunability in terms of porosity, pore size, and filament diameter, though extensive material processing leads to a higher manufacturing cost. However, their relatively soft structure can lead to damage during assembly, especially when uneven torque is applied, resulting in nonuniform thickness and altered pore properties. This, in turn, affects the homogeneity of MEA contact, particularly as contact points are often restricted to flow field ridges [7]. Considerable amount of studies highlights the importance of allowing elastic deformation in MEA to prevent breaking the catalyst layer [8-10], in some cases damaging the substrate due to high assembly compression forces. Microstructure breaks lead to worsened catalyst utilisation and loss of its lateral current conduction properties [11]. Schuler et al. present catalyst layer surface post operando scanning electron microscope (SEM) images and identify tension-induced micro-cracks and fractures caused by compression of a membrane with Ti fibres felt [12]. Nevertheless, further optimisation of the contact between the felt and the flow field is still required.

Another widely used PTL material for AEMWE is Ni-foam [13–16]. Park et al. report the effects of material and pore size of felts and foams in AEMWE, showcasing nickel materials undeniably outperforming Ti and ss [17]. Compared to felts, foams offer superior gas transport and compression distribution, while being more cost-effective and offering great tunability, not only in the morphology of the porous structure but also in thickness. However, foams also present notable drawbacks. Their sharp pore structure poses potential risks, as membrane swelling can cause the anion exchange membrane (AEM) to creep into the pores, increasing the likelihood of exposure to sharp edges and potential micro-punctures of the AEM. Additionally, their uneven surface and higher porosity contribute to increased ohmic resistance, as highlighted in a comparative study where nickel felt outperformed nickel foam in maintaining optimal conductivity and overall cell performance [18]. Furthermore, foams share mechanical vulnerabilities with felts, including susceptibility to deformation under compression. This plastic deformation can alter pore size and distribution, affecting electrolyte flow and gas transport, particularly in regions where the foam contacts the flow field ridges.

Weaved or expanded meshes, traditionally employed in AWE, are also gaining popularity in membrane technology electrolysis due to their structural rigidity and durability. However, optimising their interaction with the AEM remains challenging, and higher ICR is commonly observed in these configurations. More recent innovations include sintered stacked meshes, which entail layering of different meshes to create porosity or pore diameter gradients, while these rigid, fused meshes have demonstrated improvements in mechanical stability and mass transport, lowering the costs of processing and reducing ICR remain challenging. Additionally, researchers are exploring the incorporation of microporous layers to improve the MEA contact and designing PTLs with variable porosity gradients to enhance gas-liquid separation and electrolyte flow within the cell [19–23].

The correlation between PTLs and flow fields is also critical to cell performance and should be considered when designing a PTL. Traditional sintered metal fibre felts may suffer from structural deformation under compression, which increases tortuosity, reduces permeability, and causes nonuniform compression forces. The peak compression forces at the rib/channel interface can damage PTL fibres, leading to catalyst layer delamination and a disruption of the planar electrical connection with the electrode. This results in inefficient catalyst utilisation and performance degradation [24, 25]. Similarly, PTLs like carbon paper may also deform or break over time, accumulating in flow fields and exacerbating mass transport problems [26–28].

While some studies have explored the influence of PTL properties on performance in PEM and AWE systems, and limited work has addressed porosity-performance relationships in AEMWE, our study provides a more comprehensive investigation. We examine a novel PTL structure-knitted wire mesh (KM) as an interlayer—and its influence on electrochemical performance. Additionally, we incorporate advanced simulations based on 3D imaging of real samples, analysing thermal, electrical, and flow properties to deliver deeper insights into the interplay between PTL structure, mechanics, and performance in AEMWE. Furthermore, there is limited research on developing PTLs that allow for elastic deformation, which would better accommodate compression forces while maintaining functionality. Another key challenge lies in optimising the PTL-flow field interface, particularly in managing how the PTL interacts with the rib/channel structure to ensure uniform compression. To address these challenges, this study aims to develop novel PTL structures that incorporate customisable material properties and morphologies, allowing for elastic deformation and optimised interaction with the flow field. The goal is to create a multifunctional PTL solution that not only improves performance but also reduces cost. By advancing PTL design in this manner, we aim to bridge the gap between current limitations and the need for scalable, efficient solutions in AEMWE.

To address the outlined challenges, this study investigates a novel approach to PTL design: the use of KM, as a compressible, multifunctional interlayer within a stacked PTL configuration depicted in Figure 1B. A detailed visualisation of the stacked PTL concept comprising felt, KM, and expanded mesh (EMX), which acts as a flow field, is shown in Figure 1C. Unlike conventional foams or rigid metal meshes, the knitted mesh structure introduces a spring-like mechanical behaviour that ensures uniform compression distribution across the MEA. This allows for both enhanced catalyst contact and reduced ICR. The design leverages the inherent elasticity, structural integrity, and tunable morphology of knitted materials-offering a customisable PTL architecture that adapts to cell compression without compromising performance. Additionally, KMs are costefficient to produce, avoiding energy-intensive manufacturing while offering control over filament diameter, porosity, and thickness—influencing the elasticity.

This study is the first one to introduce a mechanically adaptive PTL design for AEMWE that directly addresses the limitations of rigid PTL-flow field interfaces. By applying an adaptive knitted interlayer, we bridge electrochemical and mechanical design principles to develop a PTL that actively responds to cell compression dynamics. The knitted mesh not only distributes mechanical stress evenly but also facilitates flow and electrical

contact, enabling the elimination of traditional flow field structures. This redefines the role of the PTL in low-temperature electrolysis systems—from a passive gas-liquid interface to an active structural and functional element, advancing the path toward scalable, efficient, and cost-reduced AEMWE systems.

This study aims to optimise cost and improve performance in AEMWE by evaluating the electrochemical and mechanical performance of novel, multifunctional Ni and Inconel KM-based PTLs. Through single-cell measurements, we assess their ability to maintain uniform compression, enhance contact resistance, and operate without machined flow fields. The goal is to demonstrate that knit mesh structures offer a viable, efficient, and scalable alternative for next-generation electrolyser designs.

2 | Results and Discussion

2.1 | Microstructural and Computational Analysis: Foundation of PTL Performance

This section portrays visual representations of KM and supports the reader with production-related outlook to relay a wellrounded sense of functionality of the metal structure as a PTL. A selection of viable structures was carried out based on available literature and our own research. All eight KM variants are presented in Figure 2A, giving an overlook of the structural variations and their denominations. The top row presents nickel samples (labelled as KMN and a number) and the bottom row Inconel 601 (labelled KMI and a number); from left to right, the targeted porosity (free volume) increases, reflected in the denomination number 1-4. All samples share the same knit wire thickness, with a singled-out wire highlighted in Figure 2E. The filaments are produced by wire drawing through a die orifice with a 125 µm diameter opening, resulting in plastic deformation of the material visible on the SEM magnified images as lines along the filaments. Notably, small material chips found on the wires can be attributed to solid-state welding of the flakes onto the filament, due to friction heat dissipation during the extrusion process. After the filament is produced, the wire is stitched on a knitting machine to create a knitted structure. The mesh can then be crimped if required and is then folded into multiple layers to fill a die tool and pressed together. The resulting structure, a pad, allows for small, elastic deformation yet still maintains its structural integrity. However, as the compression process creates a random internal structure, the porosity in any given area of the pad will be different. These randomised structure irregularities are observed in the SEM images as well. Compared to conventional serpentine flow fields, meshes exhibit significantly lower pressure drop and can distribute flow more uniformly when properly designed, leading to a ~10% performance increase for PEMFC [29]. The diamondshaped architecture of the flow field (such as our expanded mesh), in particular, allows for improved reactant and gas removal pathways and has been shown to outperform traditional single-channel serpentine patterns in both performance and pressure loss, as validated by Dong-Hui et al. [30] Additionally, the use of mesh as a combined flow distributor and PTL contributes to a substantial reduction in overall system cost by eliminating the need for separate flow fields and reducing machining complexity in bipolar plates. Furthermore,

numerous applied studies have been conducted to research the impact of knitted meshes on flow conditions. They are shown to efficiently and uniformly distribute the flow [31]. As a result, such KM potentially ensures a more consistent electrolyte flow across the in-plane of the cell at the MEA interface, reducing significant divergence in flow patterns.

We used microscopic computed-tomography (µCT) scans to obtain a 3D representation of all KM samples to parameterise the novel PTL structures. The results were used to determine porosity and served as data input for structural, electrical, thermal, capillary-pressure, and flow simulation in the software GeoDict. The computed porosity values are summarised in Table 1. It must be noted that the measured porosity can only be attributed to the local resolution of the sample, which, due to the pad production process, may not be the representative value. Therefore, we will refer to it as locally resolved porosity to differentiate it from the targeted, sample-averaged porosity. The porosity was determined using GeoDict's porosity algorithm, which is designed to correspond to mercury porosimetry (PoroDict-Porosimetry). This algorithm accounts for the connected porosity. For the evaluation, the structure was cut to receive a planar connection to the domain boundaries.

All eight PTLs, four made from Ni (PTL KMN1–4) and four of Inconel 601 (KMI1–4), were evaluated for application in AEMWE. The key parameters evaluated include relative diffusivity, tortuosity, electrical conductivity, electrical resistivity, and thermal conductivity. Table SI2 details the structural parameters of all samples, simulated in GeoDict in *x*-, *y*-, and *z*-directions.

Given that the y-axis corresponds to the through-plane, which is critical for connecting the MEA to the current collector. It directly affects electron transport, gas diffusion, and heat dissipation between the catalyst layer and the current collector. Hence, the through-plane transport properties are of more significance. Nevertheless, x- and z-directions remain important, as they correspond to the directions of electrolyte flow through the cell. The comparison among Ni and Inconel-based samples revealed a notable trade-off between gas transport efficiency and electrical and thermal performance. It is evident that higher porosity correlates with lower electronic and thermal conductivity, which aligns with common expectations, thus verifying the simulation (Figure 2C). The simulated conductivities are high in all directions, with a notably higher value in the z-direction. This high through-plane conductivity is primarily attributed to the extensive contact areas between the Ni/Inconel fibres. The simulated tortuosity decreases as porosity increases, which aligns with expectations for both the Inconel and Ni structures (Figure 2B). Additionally, all properties display a directional dependence, likely due to the weaving orientation. Upon calculating diffusion through the different fibre structures, it was found that the tortuosity is significantly lower across all these structures than that is typical for a PTL [32]. The representative capillary-pressure curves for sample KMN1 are presented in Figure SI3 for all x-, y-, and z-directions. Figure 2D compares oxygen saturation across all Ni samples (KMN1-4) at pressures of 500 and 1000 Pa, based on capillary-pressure curves. Additionally, Figure SI2 provides a similar visualisation of the saturation distribution across all Inconel samples (KMI1-4). The results indicate that higher porosity enables high oxygen saturation at

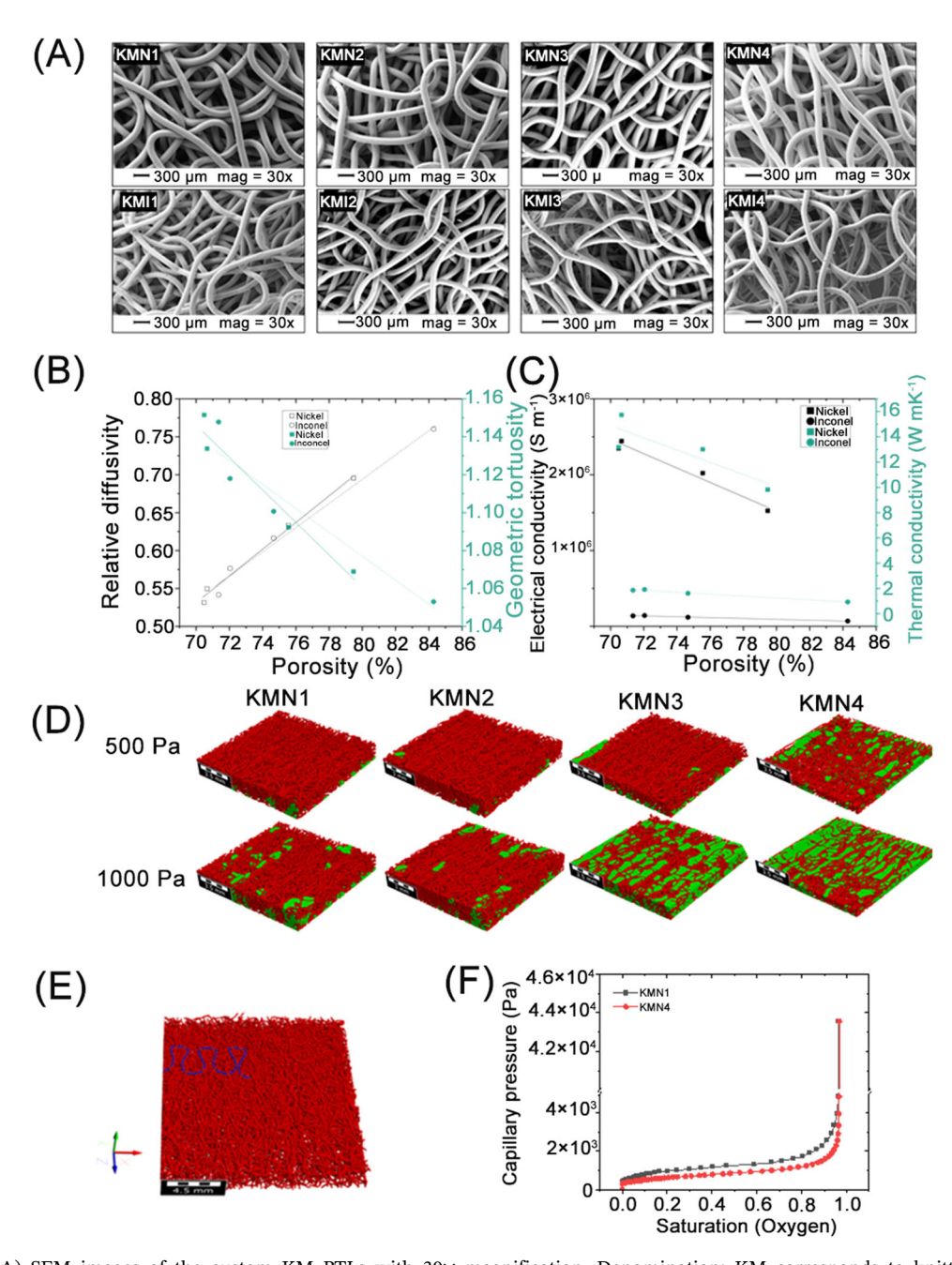


FIGURE 2 | (A) SEM images of the custom KM PTLs with 30× magnification. Denomination: KM corresponds to knitted mesh; top row N-nickel; bottom row I-Inconel; number corresponding to structure variation by porosity. The influence of porosity on (B) relative diffusivity and geometric tortuosity, and (C) electrical and thermal conductivity. (D) GeoDict simulated oxygen distribution at 500 Pa (top) and 1000 Pa (bottom) for all nickel KM structures; porosity increase direction: left to right. The mesh structure is shown in red and oxygen in green. (E) 1.5 cm × 1.5 cm, GeoDict 3D structure with highlighted single filament/wire. (F) Capillary pressure curves for oxygen saturation of the two most different nickel structures—KMN1 and KMN4.

lower pressure throughout the mesh structure (Figure 2F). The visualised oxygen distributions are promising, suggesting that increased porosity, despite lower conductivity, may enhance performance by facilitating oxygen transport.

Overall, nickel-based PTLs generally exhibited superior properties in facilitating efficient electron transfer from the current collector to the catalyst layer and efficient heat dissipation. Notably, Inconel sample KMI4 showed the highest throughplane diffusivity (0.752) of all the PTLs, indicating superior gas/electrolyte transport at a trade-off with lower electrical and

thermal conductivity. The simulated results and electrochemical performance data will serve to establish which of the parameters of the trade-off are more critical.

2.2 | Mechanical Characterisation: Evaluating Structural Integrity

In the context of AEMWE cell performance and durability, the mechanical characteristics of the cell assembly warrant particular attention, especially when considering novel PTL

TABLE 1 | Established porosity values via different methods.

Sample reference	Avg. thickness in the cell assembly @ 0.2 N m	μCT resolved 3D structure porosity 2 × 2 cm ²	GeoDict simulated in-plane porosity 1.5 × 1.5 cm ²
KMN1	2.1 mm	67.2%	70.48%
KMN2	2.0 mm	67.8%	70.66%
KMN3	1.7 mm	73%	75.55%
KMN4	1.4 mm	80.0%	79.46%
KMI1	2.7 mm	69.2%	71.35%
KMI2	2.0 mm	67.2%	72.05%
KMI3	1.7 mm	71.2%	74.66%
KMI4	1.5 mm	82.5%	84.29%

components. The specific considerations should include the uniform distribution of compression, maintaining structural integrity under operation, and minimising ICR. These factors are directly influenced by the physical characteristics of PTL structure, namely porosity and thickness. Achieving uniform compression distribution and minimising force peaks are crucial for maximising the area of the catalyst layer in electrical contact with the MEA ensuring its optimal utilisation. In regions where force peaks occur, the ICR drops significantly, allowing for locally high gas production, exacerbating the formation of hot spots. These hot spots raise the risk of thermal damage, ultimately compromising cell performance and longevity. Furthermore, even minor variations in compression distribution can undermine the structural integrity of the catalyst layer, leading to cracks and a loss of in-plane conductivity. High gradients of compression distribution have the potential to cause premature membrane puncturing or substrate breakage, which in turn can block the flow fields (or replace components e.g. expanded mesh) and increase mass transport problems translating to degradation of overall cell efficiency.

We verify the benefits of pressure distribution between two cell assemblies subject to the same torque-referenced compression. The assembly depicted in Figure 3A consists of an expanded mesh, a 250-µm-thick nickel felt, a two-piece pressure-sensitive Fuji paper inset, and carbon paper (CP, Spectracarb), all sandwiched between the end plates without flow fields. In contrast, the assembly shown in Figure 3B includes an additional 60% porosity nickel knitted mesh, placed between the expanded mesh and nickel felt. The inclusion of knitted mesh in the stacked-PTL configuration significantly reduces pressure peaks, as indicated by the Super Low LLW Prescale paper, thereby eliminating high gradients in pressure distribution. Additionally, the KM effectively evens out the assembly compression force, suggesting that more of the catalyst layer is in contact with the membrane. These results verify the positive impact of spring-like behaviour of the KM and are expected to bring significant improvements on the system level:

i. evening out the compression distribution and accommodating manufacturing tolerances across the MEA,

- ii. simplifying stack assembly by reducing sensitivity to uneven surfaces or slight dimensional mismatches, and
- iii. mitigating mechanical degradation by continuously adapting to long-term changes, such as membrane thinning during extended operation. This continuous adaptation ensures sustained electrochemical contact between layers and helps counteract performance losses typically associated with reduced contact pressure over time.

This elastic recovery function, much like a mechanical spring, offers a passive durability enhancement strategy and contributes to long-term performance retention. The use of KM thus adds both mechanical and electrochemical value to the system.

Furthermore, to evaluate the elastic behaviour of the KM and its impact on cell assembly, we conducted a metrology study to quantify PTL deformation and define a suitable reference torque for subsequent electrochemical tests. Assemblies comprising expanded mesh (EXM) and each KM variant were compressed between end plates at three torque levels: 0.2, 0.45, and 0.6 N m. The torque of 0.2 N m was the minimum clamping force necessary to secure the cell and prevent any movement within the assembly, while 0.45 and 0.6 N m were chosen to explore the optimal compaction level. Figure 3C shows the stacked PTL thickness variation across seven points of the cell assembly under the different torques and Figure 3D presents the total PTL thickness decrease between 0.2 and 0.6 N m, offering insight into the extent of deformation.

The stacked PTL design aims to provide integrative insight into the mechanical response of elastic components within meshbased flow field configurations. The applied forces in such assemblies not only are perpendicular to the KM plane but also introduce apparent bending torques at the EXM-KM interface. These bending effects have a more pronounced influence on the structural integrity of the KM compared to assemblies without an expanded mesh. The rigidity of the KM is influenced by its thickness, which must be carefully selected to balance elasticity and support. This mechanical adaptability is especially beneficial in cell setups with flow fields, expanded meshes, or rough surfaces, as the KM deforms to conform to surface irregularities, improving contact uniformity. While both Ni foam and KM can deform under compression, they behave differently: Ni foam undergoes plastic deformation, whereas the KM retains elasticity and reversibly deforms. This enables it to adapt throughout the cell's operational life, compensating for changes such as membrane thinning, maintaining even compression, and enhancing long-term performance.

A torque of 0.6 N m generally led to lower thickness variations; however, thin, high-porosity samples like KMN4 and KMI4 showed wide deviations in minimum and maximum values, likely due to KM structure bending into the EXM channels. This variability is undesired as it could lead to high assembly compression gradients and cause membrane puncturing. Therefore, a torque of 0.45 N m was selected for electrochemical testing, balancing sufficient compaction with minimal structural irregularities.

Further deformation data for KM alone is available in the Supplement Information (Figure S17). It is evident that when

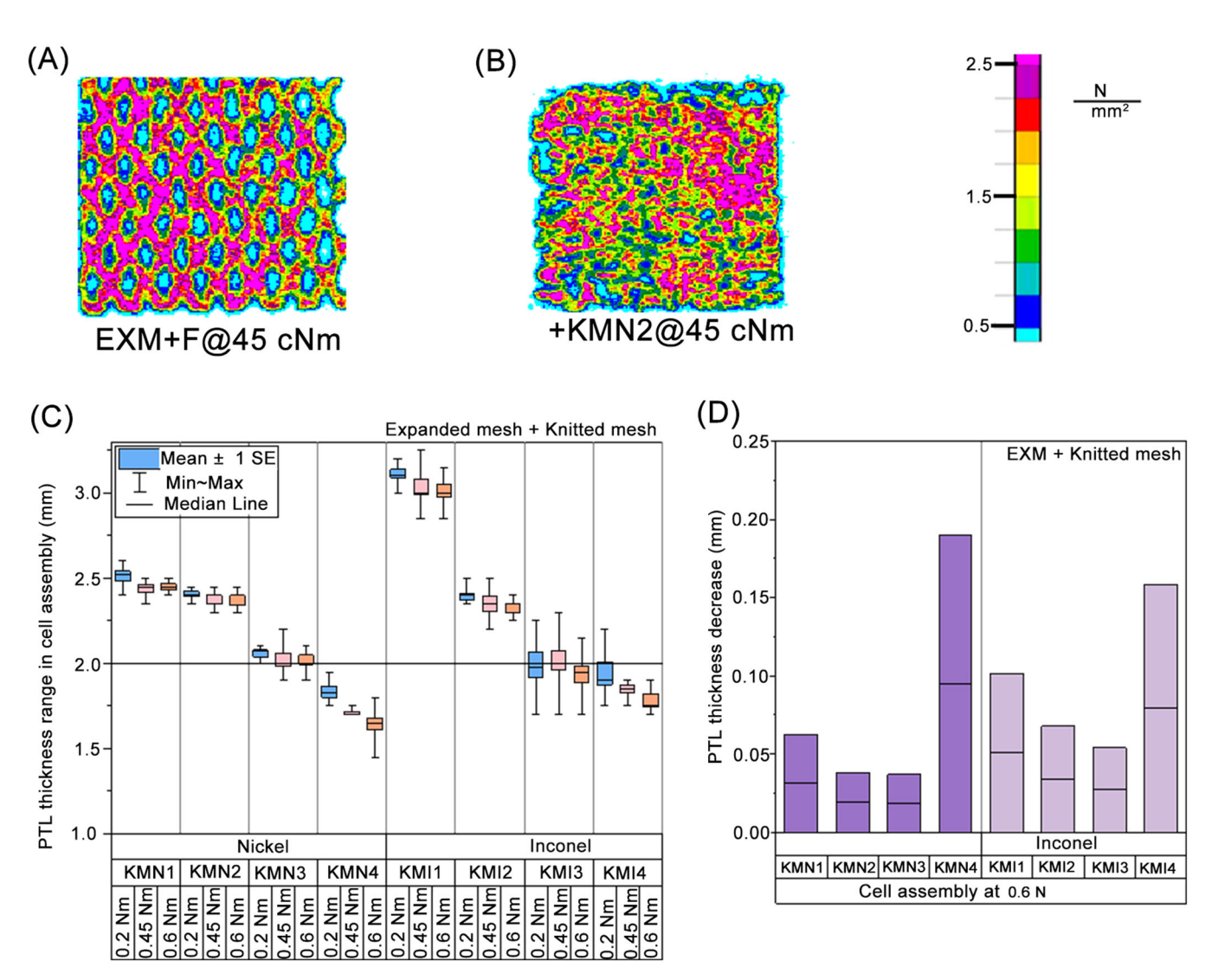


FIGURE 3 | Fuji pressure sensitive film obtained from $4 \,\mathrm{cm}^2$ cell assembly with $4 \times M4$ screws tightened with 0.45 N m reference torque (also the operation point for acquired electrochemical data): (A) EXM + felt + 2-piece Prescale film + CP; (B) EXM + KMN2 + felt + 2-piece Prescale film + CP. (C) Results of the stacked PTL thickness variation, measured at seven points across the cell assembly under the three selected compressions for all knitted meshes selected for this study. Averaged setup torque to compression transformation: $0.2 \,\mathrm{N}$ m-85 N cm⁻², $0.45 \,\mathrm{N}$ m-190 N cm⁻², and $0.6 \,\mathrm{N}$ m-250 N cm⁻²; (D) total PTL thickness decrease between the reference torques of $0.2 \,\mathrm{and} \,0.6 \,\mathrm{N}$ m applied during assembly compression.

only perpendicular forces are applied to the KM plane, PTL deformation increases with the increase of free volume, directly correlating with the sample's through-plane stiffness. However, high-porosity Inconel-based samples showed greater variability due to the bulky, folded structures required to achieve porosity. Notably, sample KMI1 (~70% free volume) deviated from the deformation trend, attributed to its increased hardness and thickness, which led to partial, meta-stable compression.

Other studies on PTLs have also highlighted the significance of ICR, as it plays a crucial role in the overall performance of electrolysis systems. For instance, Razmjooei et al. reported that at an assembly pressure of $200\,\mathrm{N\,cm^{-2}}$, the ICR values for stainless steel PTLs (ssPTL) were in the range of 65–70 m Ω cm². However, when a nickel microporous layer (NiMPL) was applied to the ssPTL, the ICR significantly decreased to approximately $20\,\mathrm{m}\Omega\,\mathrm{cm^2}$, demonstrating the benefits of using microporous coatings [20]. Similarly, Stiber et al. found that

under the same compaction pressure, the ICR for ssPTL was approximately $75\,\text{m}\Omega\,\text{cm}^2$, but this resistance was reduced when a titanium microporous layer (TiMPL) was applied, with the TiMPL-ssPTL reaching an ICR of $50\,\text{m}\Omega\,\text{cm}^2$ [33]. These findings reinforce the importance of optimising the PTL structure and surface coatings to improve interfacial contact, which is critical for enhancing the efficiency of electrolysis systems.

The reference sample used for ICR measurements in this study consists of both EXM and felt, which are made from nickel. As such, the system primarily exhibits bulk resistance, with ICR being negligible due to the same material at the contact points. Thus, the reference value reflects the combined ICR between the gold-coated copper and nickel EXM, as well as between the nickel felt and gold-coated copper. Then, a KM layer was introduced between the EXM and felt. For KM, since the material is also nickel, the interfacial resistance remains negligible, and the observed increase in ICR is attributed to a rise in

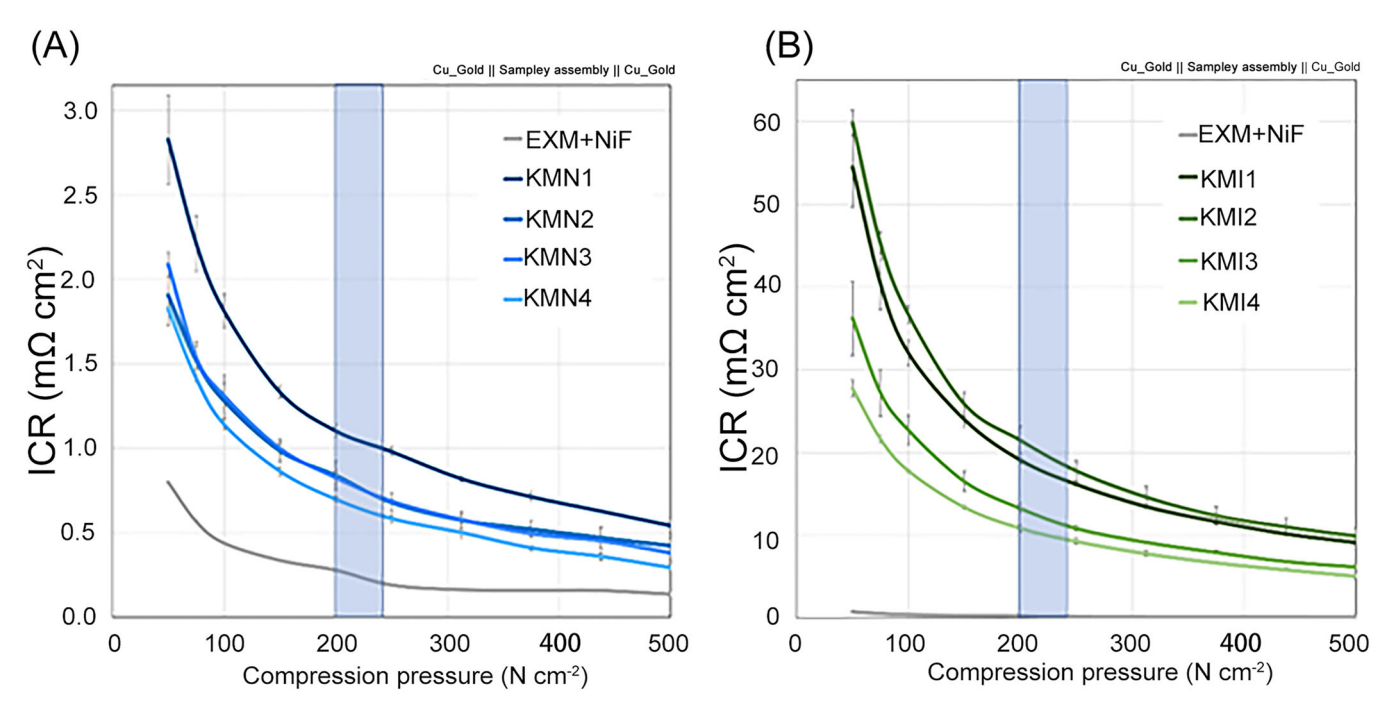


FIGURE 4 | ICR as a function of assembly compression pressure, measured using gold-coated cylinder blocks. The highlighted region represents the standard cell assembly in an electrolysis stack. (A) Reference measurements of EXM and Ni-felt, as well as nickel samples KMN1–4, each placed between the EXM and Ni-felt and (B) measurements including Inconel samples KMI1–4.

bulk resistance. This correlates with the results presented in Figure 4, where higher porosity samples exhibit lower ICR, while variations correspond to differences in the 'local porosity' of the ICR samples.

The advantage of the all-nickel setup can be explained by the superior electrical conductivity of Ni compared to Inconel (summarised in Table SI1-2), directly influencing the ICR outcomes. Nonetheless, the ICR results for the stacked PTL system—comprising nickel EXM, Inconel KM, and nickel felt—are comparable to those of single-component NiMPL-ssPTL, achieving values of approximately 20 m Ω cm 2 when using KNI1 and KNI2 (with < 70% porosity). This is noteworthy, given that Inconel and stainless steel exhibit similar electrical conductivity, highlighting the significant role of the knitted mesh structure itself in reducing ICR. Even more promising is the ICR result for KMI4, which, with its 85% porosity, further halves the ohmic resistance of the stacked PTL, yielding an exceptionally low ICR of $10 \, \text{m}\Omega \, \text{cm}^2$.

2.3 | Electrochemical Characterisation: Performance Analysis in AEMWE

This section presents a comprehensive analysis of the electrochemical performance of the studied PTLs in AEMWE, focusing on polarisation curves, electrochemical impedance spectroscopy (EIS), and equivalent circuit fitting (ECF). The results, including figures and supplementary data, are used to correlate key electrochemical parameters with the structural and mechanical properties discussed earlier, providing insights into the optimal conditions for enhancing cell efficiency and durability.

The cell assembly and parameters used in this study are detailed in the experimental section and summarised in Table S13.

Several methodological considerations were made to ensure a focused and comparative evaluation. An EXM was selected as the flow field to align with current literature and state-of-the-art designs, including sintered meshes, facilitating direct comparison. The study concentrates exclusively on the anode PTL, with no optimisation of the cathode side, to prevent overlapping factors that could influence performance. To further reduce variability from kinetic efficiency, the anode catalyst-coated substrate (CCS) was prepared with a high nickel loading. Likewise, high platinum loading (0.8 mg_{Pt} cm⁻²) was used at the cathode to ensure that it would not become a limiting factor. Additionally, 1 M KOH electrolyte concentration was chosen to minimise the influence of electro-kinetic limitations on the cell performance (for electrolyte concentrations < 0.5 M KOH) [19, 34], maintaining consistency across experimental conditions. The electrochemical characterisation followed an established activation and breaking-in protocol to assure that all data were extracted at the same operating condition and are therefore representative. The extent of these protocols is described in the experimental section. Figure 5A presents recorded polarisation curves and high frequency resistance (HFR) corrected plots for Ni samples; similarly, Figure 5B shows performance curves for Inconel samples.

To establish a reference for performance, we first evaluated cells without the knitted mesh (Figure 5A, pink and black curves) using state-of-the-art MEAs and conventional flow fields. Two PTL configurations were tested: the commercial Ni felt (2Ni06-020) and a modified Ni felt of the same thickness, but asymmetric porosity, where the denser side is in the interface with the catalyst (Ni-LP/HP-250). Between the cells without the KM in assembly, the performance of Ni-LP/HP-250 is better, reaching $2.09~{\rm A~cm}^{-2}$ at $2~{\rm V}$. This is attributed to the better utilisation of the catalyst layer at the denser side of the felt. These results

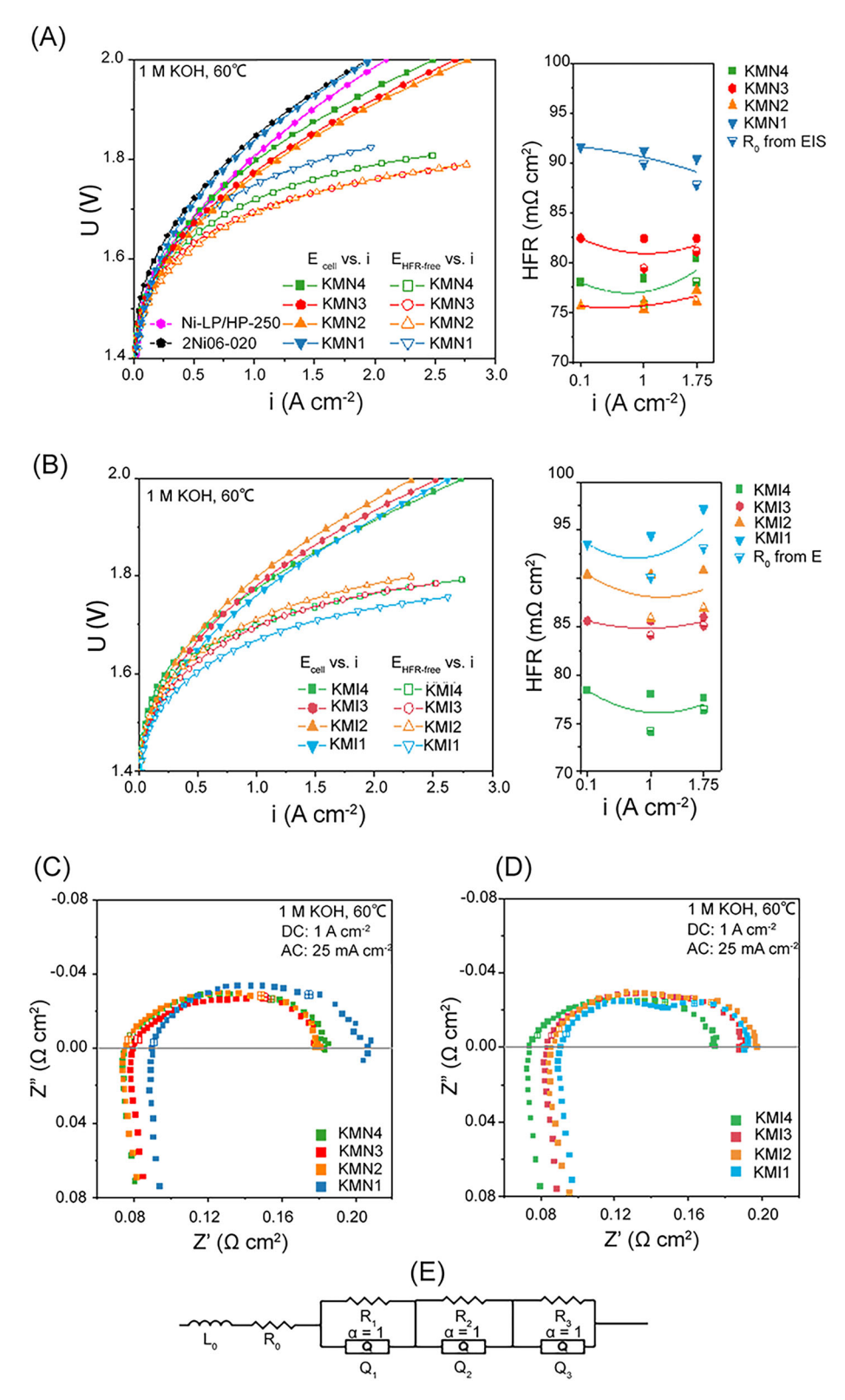


FIGURE 5 | Polarisation curves and high frequency resistance response recorded at three currents: (A) cells with nickel KM samples. (B) Cells with Inconel 601 samples. EIS represented as Nyquist plots, recorded at $1 \, \text{A cm}^{-2} \pm 25 \, \text{mA cm}^{-2}$. (C) KMN1-4 samples. (D) KMI1-4 samples. Hollowed points represent frequency values of 100 Hz for cross and 10 kHz for vertical lines, between which gas evolution resistances of the anode and cathode are superimposed. The impedance values recorded at frequencies lower than 100 Hz are widely attributed to mass transport. The EIS analysis of this study is supported by the publication of Ranz et al., on the AEMWE loss mechanisms they attribute to specific parts of the spectra [35]. (E) Layout of the used ECF model. L_0 = impedance of the electrical connection; R_0 = ohmic resistance intercepted at the high frequency; R_1 = HER resistance, charge transfer resistance accompanied with double layer effects in the electrode (Q_1); R_2 = OER resistance, and charge transfer capacitive effects (Q_2); R_3 and Q_3 correlating to mass transport phenomena.

highlight the performance ceiling attainable through conventional PTL tuning alone.

To contextualise the performance enhancement achieved with our PTL design, we compared our results with relevant literature employing the same functional components, namely the Fumasep FAA3-50 membrane, and comparable operating conditions (1 M KOH, 60°C). In a study by Liu et al., a completely platinum group metal (PGM)-free configuration (NiFe₂O₄ anode and NiFeCo cathode, 2 mg cm⁻² loading each) was tested under the same operating conditions. Their system achieved 2.4 A cm⁻² at 2.2 V [36]. In another study by Gatto et al., an IrO₂ anode (3 mg cm⁻²) and a Pt cathode (0.5 mg cm⁻²) were employed. Despite the high noble metal loadings, the cell operated at 2 A cm⁻² with a cell voltage of 2.2 V under 1 M KOH at 60°C—comparable to our baseline configuration without the knitted mesh and PGM-free anode [37].

This clearly demonstrates that the substantial impact PTL design can have on electrochemical performance, even when other cell components and/or operating conditions are held constant. Thus, our baseline results (the reference cells without KMs, Figure 5A) already match the current performance frontier AEMWE systems with reduced reliance on PGM materials.

Ultimately, the addition of a KM to the stacked PTL structure enhances performance, particularly when combined with more porous structures. This is primarily due to not only improved compression distribution across the PTL but also reduced mass transport resistance. This effect outweighs the impact of the slight increase in contact resistance compared to the combination of EXM and nickel felt, as seen in Figure 5B. In the case of KMI1 (< 70% porosity), the polarisation curve shows a noticeable upward bend, suggesting the onset of mass transport limitations at higher current densities. This behaviour is likely due to the increased sample thickness relative to other KMs. Despite having the highest R_0 value, attributed to its relatively lower porosity, the corrected polarisation curve for KMI1 shows the best performance. The superior performance of KMI1 compared to KMN1 may be explained by the heat transfer dynamics through the PTL. The thicker Inconel structure (approximately 20% thicker, as shown in Figure 3C) has a lower thermal conductivity compared to Ni (Table SI1 and computed GeoDict values in Table SI2), leading to higher temperatures at the MEA. Similar findings were reported by Weber et al., who demonstrated that reduced heat transfer coefficients in PTLs can lead to elevated local temperatures at the MEA, subsequently enhancing performance [7].

When excluding the least porous and thickest porous knitted meshes (KMI1 and KMN1), an interesting trend emerges: Inconel samples exhibit a decline in performance as porosity decreases, whereas nickel samples display the opposite trend. This could be linked to differences in the thermal conductivity, which merits further investigation.

The EIS data presented in Figure 5C,D generally correlate with the ICR results in Figure 4, confirming that lower R_0 values are associated with the higher elasticity of knitted meshes. While both parameters reflect interfacial resistance, it is important to note that the high-frequency resistance is acquired during cell

operation and reflects additionally the resistance to electron flow through the system, including the electrolyte. In highly alkaline electrolytes, such as it is in this study, the electrolyte conductivity promotes the electron flow within the PTL structure and lowers the HFR. The relationship between the ICR and the HFR would be more prominent with a neutral pH electrolyte. Overall, the impedance data align with the trends observed in the polarisation curves. Notably, the sample KMN2 (70% porosity) behaves similarly to KMN3 (75%), which is also reflected in the ICR data (Figure 4A) and corresponding HFR. This similarity explains the comparable polarisation curves for these samples (Figure 5A). However, KMN2's slightly higher mass and greater thickness (Figure 3A) suggest that its marginally improved performance compared to KMN3 may stem from electrochemical reactions occurring on the surface of the KM itself.

From a design perspective, reducing both the volume and mass of the electrolyser components is often desirable. Therefore, KMN3, with 75% porosity, is recommended as the optimal PTL among the nickel knitted mesh samples.

In the case of the Inconel samples, the EIS data in Figure 5D reveal a pronounced semicircle at low frequencies, indicative of mass transport limitations. This effect becomes more pronounced as porosity decreases. To better understand these results, further analysis using ECF was necessary to determining whether mass transport (MTX) resistances are also present in the nickel samples but are masked by the resistances from electrochemical gas production reactions.

To further interpret the EIS data, we employed an ECF model using the layout $L_0 sR_0 s(Q_1 pR_1) s(Q_2 pR_2) s(Q_3 pR_3)$ presented in Figure 5E, resulting in three distinct semicircles in the impedance spectra. The first resistance, R_0 , corresponds to the ohmic resistance, which is closely tied to the ICR as previously discussed. The second resistance, R_1 , represents the hydrogen evolution reaction (HER) resistance. However, this semicircle is often superimposed with R_0 and R_2 , making it difficult to accurately deconvolute due to inherent ECF fitting errors. The third resistance, R_2 , is associated with the oxygen evolution reaction (OER). While R_2 is partially superimposed with both R_1 and R_3 , its larger magnitude $(R_2 \gg R_1)$ makes this superposition less significant. Finally, R_3 corresponds to MTX resistance, which appears in the low-frequency region and is prone to measurement inaccuracies, leading to the highest fitting error in the ECF. Overall, the circuit fitting was performed with an error range between 0.88% and 1.51% and the fitted resistance values can be found in the Supplement Information in Table SI4.

- R_0 (ohmic resistances): The fitted R_0 values have a clear correlation with ICR results indicating a strong influence of the sample morphology on the resistance, undermining however the importance of electrical conductivity in the overall cell resistance. As seen in Figure 4, the Inconel samples showed 20-fold worse ICR values. This is not translated to the R_0 results.
- R₂ (OER resistance): Despite similar porosity and thickness (e.g., KMN1 vs. KMI2 or KMI3 vs. KMI4), R₂ values are lower for nickel samples compared to Inconel. This slight difference might be due to the OER occurring on the

PTL surface, with nickel showing higher activity than Inconel 601. However, this variation has minimal impact on overall PTL performance. Interestingly, the thicker KMI1 (2.7 mm) sample exhibits a lower R_2 value compared to KMI2 (2 mm), potentially due to increased temperature at the MEA interface, which could enhance OER kinetics. Therefore, the KMI1 result represents a poorly designed PTL with suboptimal thermal management properties.

R₃ (MTX resistance): As porosity increases, R₃ decreases.
 This is consistent with oxygen saturation trends observed in simulations conducted in this study. Ni samples generally show lower MTX resistance than Inconel, which is equally corroborated by simulation results.

The total resistance $(R_0 + R_1 + R_2 + R_3)$ aligns closely with the trends observed in the polarisation curves, confirming the validity of the ECF model for interpreting the overall cell performance. A clear pattern emerges, showing a reduction in total resistances with increasing free volume, supporting the notion that porosity plays a crucial role in minimising electrochemical resistance. The thinnest and most porous Inconel sample (KMI4) demonstrates the lowest total resistance, highlighting the performance benefits of optimised PTL structure and morphology.

2.4 | Integrative Analysis: Correlating Structure, Mechanics, and Performance

Advancing AEMWE technology can benefit significantly from optimising the PTL interlayer structure. Our simulation results highlight a trade-off between microstructural features—diffusivity, and through-plane conductivity—that must be balanced for optimal performance. Notably, PTLs based on knitted meshes offer a promising solution, as their structure supports both electrochemical efficiency and mechanical robustness.

The mechanisms underlying the performance enhancement arise from two distinct functionalities of the proposed PTL-flow field structure. Firstly, the elasticity of the knitted mesh enables more uniform pressure distribution across the cell area. This not only reduces regions of excessively high compaction force but also contributes to overall pressure homogenisation across the sample. Such redistribution directly improves the contact between the catalyst layer and the membrane, enhancing catalyst utilisation and, consequently, the overall cell performance. Furthermore, minimising localised forced maxima mitigates the occurrence of high current density zones, which are often responsible for hot spots and mechanical degradation of the membrane electrode assembly.

The second key mechanism involves the improved flow characteristics of the knitted mesh, provided that appropriate design parameters are selected. Our simulation study demonstrates that knitted meshes exhibit excellent permeability, flow and structural characteristics, facilitating efficient removal of product gases and alleviating mass transport limitations. This effect is also corroborated by our electrochemical measurements, where the absence of a knitted mesh results in upward bending of the polarisation curve—a signature of mass transport losses—that is significantly reduced upon mesh inclusion.

Finally, the continuous single-wire design, which folds upon itself and multiplies contact points in all directions, results in excellent electrical and thermal conductivity in nickel-based samples and very good performance in Inconel-based ones, as confirmed by simulation studies. Importantly, the inclusion of the knitted mesh does not introduce measurable increases in cell resistance, despite being an additional component in the assembly.

As illustrated in Figure 6A, the spring-like behaviour of the KM interlayer ensures dynamic compression distribution and contributes to the observed ICR improvements. This mechanical adaptability is a cornerstone of the multifunctionality offered by stacked PTLs. This analysis includes a closer examination of structural differences, particularly porosity as influenced by the

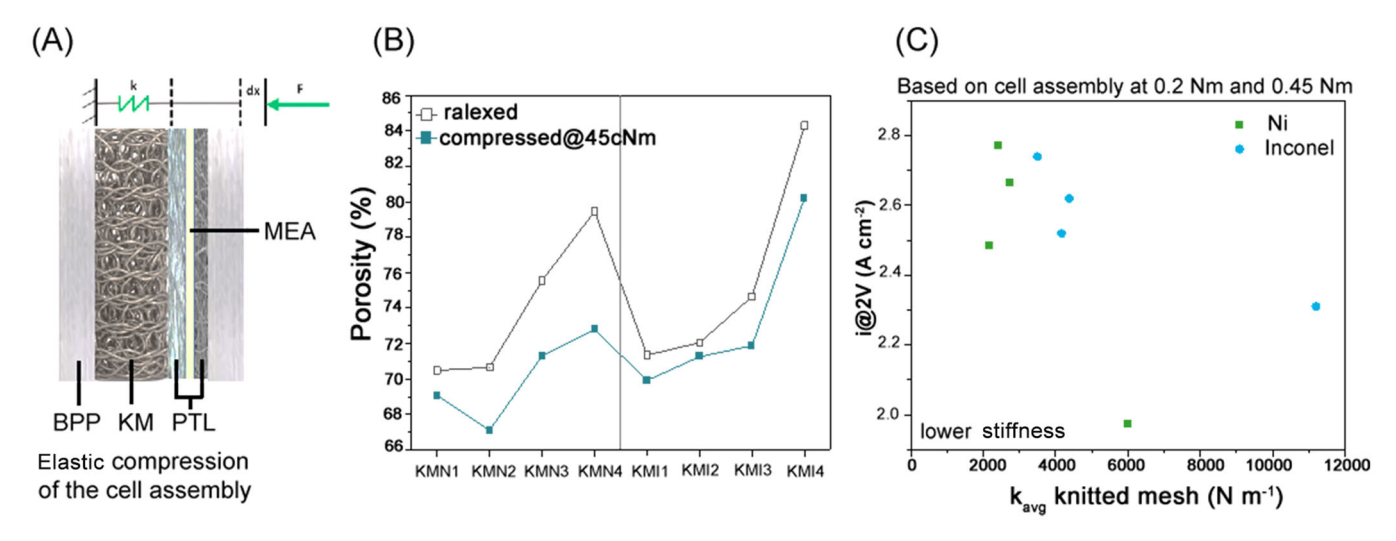


FIGURE 6 | (A) Adaptability of knitted mesh structures under assembly compression. (B) Comparison of the knitted wire mesh pads in relaxed and compressed states illustrating the impact on porosity. (C) Correlation of the performance indicator with sample average spring stiffness (k_{avg}). The k_{avg} was calculated between the average sample height at 0.2 N m assembly and 0.45 N m.

pad's spring stiffness, showcased in Figure 6B. Notably, KMN2, which exhibits significantly greater elasticity than KMN1, more effectively distributes mechanical compression across the cell. With approximately double the elasticity of KMN1, KMN2 enhances the uniformity of MEA contact and increases the number of catalyst utilisation areas, thereby improving electrochemical interface conditions. Overall, the ICR results showcase that the selected materials exhibit significantly lower values than those reported in the literature so far. The stacked PTL assembly with Inconel KM as the interlayer achieves ICR values comparable to single-component NiMPL-ssPTL (~20 mΩ cm²), with even further reductions to $\sim 10 \,\mathrm{m}\Omega\,\mathrm{cm}^2$ observed in highly porous configurations (80%). Meanwhile, the ICR values with the Ni component are in the range of $\sim 1 \,\mathrm{m}\Omega\,\mathrm{cm}^2$ at $200\,\mathrm{N}\,\mathrm{cm}^{-2}$, showcasing structural and material synergies in minimising resistance. Figure 6C demonstrates that lower spring stiffness (k) correlates with improved performance. Samples with reduced stiffness offer better compression distribution and reduced ICR, aligning with the observed performance trends.

Electrochemical characterisation, including polarisation curves, EIS, and ECF analyses, indicates that nickel-based PTLs with higher porosity (> 70%) and elasticity provide superior performance. This improvement is attributed to reduced ICR and beneficial oxygen saturation, which inhibits MTX resistances. Conversely, the best-performing Inconel sample KMI4 is the thinnest and exhibits the highest porosity. This suggests that Ni materials may exhibit a less pronounced trade-off between the electrical conductivity (improved at lower porosities) and gas permeability (enhanced at higher porosities). For Inconel, limited gas permeability leads to more pronounced MTX resistances, as observed in the EIS semicircle at low frequencies. Therefore, higher porosity structures with high diffusivity and low tortuosity are favourable for Inconel.

Further PTL optimisation involves reducing mass via lower porosity or thinner structures, allowing material savings without compromising on performance. Electrochemical data show that PTLs with 75%–80% porosity and reduced thickness deliver optimal performance improvement, making material reduction a viable strategy for cost-effective cell design.

In summary, KM PTLs provide several advantages due to their customisation. They support diverse material selection, with filaments diameters ranging from 0.05 to 0.7 mm, and offer tunable porosity and thickness, with a minimum thickness of ~1 mm. Their elastic nature reduces stack assembly variability and distributes peak forces homogenously compared to traditional flow field/felt interface. Additionally, KM structures support slow, uniform electrolyte flow by efficient vortex mixing. Compression performance can be tailored by adjusting the filament diameter, PTL porosity, material hardness (via heat treatment), and mesh structure (e.g., loop size). KM PTLs are cost-effective to manufacture, requiring less energy, material, and emissions. They can be produced in various shapes, including designs with integrated flow distribution channels, and are weldable to metallic components, making them versatile for PTL applications.

The PTL optimisation strategy explored in our work could be assimilated to cathodic PTL design. However, AEMWE systems

are often operated with a dry cathode, meaning that the twophase flow and water management challenges are not as prominent on the cathode side as they are on the anode. This was motivated by the well-established limitation posed by oxygen evacuation on the anode [38], which we aimed to prioritise.

3 | Conclusion

This study highlights the critical role of anode PTLs in AEMWE, focusing on structural innovations and different materials (Nickel and Inconel 601). The introduction of a low-cost KM PTL demonstrated improved compression force distribution, enhanced gas transport, and optimal electrical and thermal conductivity within the cell. This approach integrates a 'spring-like' elastic structure into the PTL assembly, ensuring mechanical stability during operation and facilitating uniform compression across the MEA.

Our findings suggest that this stacked PTL design offers a costeffective and scalable alternative by potentially reducing the need for traditional flow fields, thus simplifying cell manufacturing. While the electrochemical testing indicated improved operational metrics, the primary significance lies in the demonstrated benefits of structural optimisation. The outcome of this study provides a framework for developing adjustable, costeffective PTLs that can complement or replace existing designs of AEMWE systems.

Future research should expand on these findings by further evaluation of durability and investigation of other elastic PTL materials, advanced flow distribution mechanisms, and the potential integration of alternative spring-like elements. These developments could further enhance the robustness and efficiency of PTLs, paving the way for scalable and economically viable hydrogen production. This study concludes that KM PTLs are qualified for use in AEMWE and are now commercially available at KnitMesh Technologies (UK).

4 | Experimental Section

4.1 | Material Specification

Nickel-alloy felts: All substrates used in this study were manufactured by NV Bekaert SA (Belgium). As a reference, a commercially available felt, 2Ni06-020, was used—comprising sintered nickel metal fibres with 88% porosity and a thickness of 250 μm . Pre-commercial substrates were also investigated: sample Ni-LP-450, a sintered nickel fibre felt with lower porosity and a thickness of 450 μm ; and sample Ni-LP/HP-250, a sintered nickel fibre felt with dual porosity (low/high) and a thickness of 250 μm . Finally, for the stacked PTL design, sample Ni-LP/HP-200 was used for the CCS.

Nickel-alloy knitted meshes: All PTLs used in this study were custom-manufactured at KnitMesh Technologies (UK). All samples had 0.125 mm fibre diameter. KM1–KM4 samples were made out of Ni200; KM5-KM8 samples were made out of Inconel601. More parameters can be found in Sections 2.1 and 2.2 and in Supplement Information.

Nickel-alloy expanded meshes: All flow distributors used in this study were manufactured by SORST Streckmetall GmbH. The samples were custom-made out of Ni200 in the diamond-shape expanded mesh with a thickness of 0.5 mm and cut to size 2 cm by 2 cm.

Carbon paper: All measured cells were assembled with a commercial Spectracarb 2050A-1050 purchased at fuelcellearth.com.

Anon exchange ionomer: All measured cells used Fumasep-FAA3-50, a $50\,\mu m$ thick, non-reinforced AEM, commercially available at QuinTech. The ionomer solution was prepared by dissolving the $10\,w t.\%$ crushed membrane in analysis grade EtOH.

No-flow-field nickel bipolar plates were used and together with the cell are a proprietary concept.

4.2 | CCS Fabrication

Anode catalyst ink proportions: 9 mg Ni nanoparticles from Roth + 0.3 mL deionised water + 0.6 mL analysis grade IPA + 1 mg ionomer solution. Cathode catalyst ink proportions: 8 mg Pt-C nanocatalyst with 40 wt.% Pt from Roth + 0.3 mL deionised water + 0.6 mL analysis grade IPA + 2 mg ionomer solution. Both inks were at 15°C in ultrasonication with 100% power for 1 h. All CCS samples were batch prepared by the nitrogenfed airbrush spraying method, using an automated arm following a custom pattern to reduce variations in catalyst loading over measured cells. The vacuum heating plate, where the CCSs were placed, was set to 60°C to help evaporate the solvents. Following, the anode ink was deposited on nickel felt and the cathode ink on carbon paper. To estimate the catalyst loading yields, the mass of the pristine substrate was measured and subtracted from the mass of the substrate after catalyst layer deposition. The final catalyst lading data are presented in Table SI3. Moreover, the pristine electrode's surface, focused ion beam (FIB)-SEM model, and cross section are accessible in supplement information Figures SI7-9.

4.3 | Single Cell Components and Assembly

The Assembly: Between the KM and the catalyst layer, a PTL from Bekaert with two porosities (low/high) and a thickness of $250\,\mu m$ was used as the interlayer to avoid puncture of the membrane. The benefit of using bilayer PTLs was already discussed previously [39, 40], by multiscale modelling of gas evolution and transport through the structure. Therefore, our comparative study of 10 PTL configurations includes

- i. two variants of sintered metal fibres nickel felts + nickel single expanded mesh (acting as flow field) and
- ii. nickel felt + 4 porosity variants knitted meshes in two different materials (nickel and Inconel) + nickel single expanded mesh (acting as flow field) depicted in Figure 1B.

The AEM and CCS were activated in accordance with the manufacturer's guidelines in 1 M KOH. The assembly consisted of the following components, starting at the anode: Ni200

bipolar plate, no flow fields + Ni200 diamond shape expanded mesh + option of nickel alloy knitted mesh + option of Ni200 sintered metal fibres felt as CCS + AEM + spectracarb as CCS + Ni200 bipolar plate, no flow fields. The cell had a square-shaped $4 \, cm^2$ area compressed with 4xM4 screws torqued to $45 \, cN$ m each.

Compression distribution: To determine the right assembly torque and therefore cell's compression, a pressure-sensitive foil (Prescale) from Fujifilm was used. Both LLLW and LLW types were employed to gain insight into the impact of the PTL on pressure distribution. All obtained compression distributions were analysed by FPD-8010E-Software, a pressure mapping system. All measured cells were investigated, with the assembly resembling the operating cell, whereas instead of the AEM, the Prescale film was placed. Each assembly was repeatedly made for three torque steps, 20, 45 and 60 cN m.

PTL Deformation under Compression: To quantify the elastic deformation of the knitted mesh, a 4 cm² square pad of each sample was sandwiched between the bipolar plates—either as a standalone layer or in contact with an expanded mesh on one side, reflecting the default cell assembly. Each assembly was tightened in the same manner at three reference torque steps, and for each step, assembly thickness measurements were taken at 6 or more points throughout the cell with a manual Vernier calliper with a measurement accuracy of 0.05 mm. The deformation values were established as the difference between assembly thickness under compression with reference torque 20 cN m and the possible operation torque values (45 or 60 cN m).

Contact resistance: The ICR was recorded for stacked PTL concept, which included Ni expanded mesh + Ni-alloy knitted mesh pad (8 different samples) + Ni felt and a reference PTL concept including Ni expanded mesh + Ni felt. Each stacked PTL concept was placed between two gold-coated copper cylinders, which were located in a pneumatic manual press with a digital force reading interface. Each of the copper cylinders was electrically connected to the ZENNIUM Potentiostat from Zahner-Eelctric GmbH. Constant current of 5 A was applied and a voltage reading at each pressure point was recorded. Each measurement was repeated three times. The ICR measurement followed the protocol already described in previous report [33].

4.4 | Single Cell Electrochemical Measurements

Before the operation, the cell was flushed with a freshly prepared 1 M KOH feed for 1 h, slowly increasing the temperature to the operating point of 60°C. The electrochemical measurements were recorded with the use of ZENNIUM Potentiostat from Zahner-Eelctric. First, the activation protocol was initiated, which included a stepwise increase of voltage held for 5 min each until the maximum set potential of 2 V. The activation protocol was about 90 min of cell operation and was followed immediately by the stabilisation protocol. To ensure a steady state of the cell before recording the polarisation curves, the cell underwent a stabilisation protocol. It comprised of three 10 min cycles, and each cycle was a voltage-controlled ramp up from 1.25 to 2 V in 5 min and then a recovery from 2 to 1.25 V in the next 5 min.

During the stabilisation protocol, the cell was operated for a total of 30 min. After the activation and stabilisation protocol, each cell was kept at 1.25 V for 10 min to investigate if a short circuit was apparent. None of the cells presented in this study showed signs of a short circuit throughout the electrochemical characterisation process. Immediately after, polarisation curves were recorded under voltage increasing from 1.25 to 2 V in 20 min and backing down to 1.25 V in 20 min. Finally, reference EIS data were recorded in galvanostatic mode at 1.75 A_{DC} cm⁻² \pm 125 mA_{AC} cm⁻² and 0.5 A_{DC} cm⁻² \pm 50 mA_{AC} cm⁻² before each measurement, the cell was stabilised at the operating current for 5-10 min. The EIS results were recorded at frequencies from 100 kHz to 100 mHz. To extract the impedance values, an ECF was simulated using AfterMath software from Pine Research Instrumentation. For this, an ECF build with the following elements was used: L0sR0s(Q1pR1)s(Q2pR2)s(Q3pR3). The obtained values are present in Supplement Information.

4.5 | Morphology Characterisation Techniques

 μCT : 2 × 2 cm² PTLs' 3D geometry was obtained by means of CT using a SkyScan 2214 Nano-CT from Bruker. The measurements were conducted at an acceleration voltage of 80 kV and a source current of 0.1 mA, resulting in a resolution of 6.0 μ m/vx for all samples. The data were reconstructed using the NRecon program, also developed by Bruker.

Porosity was determined using the CTAn program (Bruker). A volume of interest was selected from the reconstructed image and the porosity was determined using binarization.

SEM: SEM was used to measure the fibre structure and appearance of the Ni electrode (pore) structure. Surface and cross-sectional imaging was done using a Zeiss Crossbeam 350 equipped with an energy dispersive spectroscopy (EDS) detector (Oxford ULTIM MAX 100 mm²). A work distance (WD) of 5 mm was maintained using a 15 kV accelerating voltage for imaging of the nickel fibre structures. Imaging of the Ni electrode was performed at 2 and 5 kV with 5 mm WD. EDS area analysis and mapping were performed at a WD of 5 mm and an accelerating voltage of 15 kV. The SEM surface measurement is shown in Figure SI7.

FIB-SEM: FIB-SEM tomography was performed to measure the porous structure of the catalyst layer in 3D. The Zeiss Crossbeam 350 FE-SEM equipped with the gallium liquid metal ion source was used for FIB-SEM operation. FIB-SEM tomography was performed to measure the porous structure of the catalyst layer. A WD of ~5.1 mm at the coincidence point between FIB and electron gun at 54° sample tilt was used for the tomography. Before cutting, platinum and carbon layers, including tracking marks, were deposited with the gas injection system on top of the electrode to enable drift compensation. A large and fine trench was prepared to expose the electrode for the imaging. FIB current of nA at 30 keV was used for slicing. A secondary electron Everhart-Thornley detector was used for imaging at 2 kV with a dwell time of 0.5 µs averaging four lines. One image of the electrode as a cross-section is shown in Figure SI9.

GeoDict: GeoDict 2024 was used for analysing the μCT fibre structures and generating a 3D structure from FIB–SEM slices (Figure SI8). First, the grayscale images were imported into a 3D model using the GeoDict ImportVol module. The images were aligned, cropped to a 1.5×1.5 cm² sample size and segmented using the Otsu algorithm. The 3D structures were thoroughly characterised to receive electronic conductivity, thermal conductivity, flow properties, tortuosity (bulk diffusion), and capillary pressure curves. For capillary pressure curves, a contact angle between the nickel fibres and water of 25° was used for all structures [41].

Acknowledgements

This paper/document was made possible through funding the HYScale project, which is supported by the Clean Hydrogen Partnership and its members under the Grant Agreement No. 101112055. Funded by the European Union. Views and opinions expressed are however those of the author(s) only and do not necessarily reflect those of the European Union or Clean Hydrogen Partnership. Neither the European Union nor the granting authority can be held responsible for them. Open access funding is enabled and organised by DLR.

Conflicts of Interest

The authors declare no conflicts of interest.

Data Availability Statement

All data supporting the findings of this study are included within the article and its Supplementary Information. The manufactured samples were thoroughly characterised, with detailed methodologies and data acquisition processes described in the Methods section. Each knitted mesh sample has a unique reference, ensuring reproducibility by the manufacturer. For additional information or specific data requests, the corresponding author is available to provide further assistance upon reasonable request.

References

- 1. S. Kang, Y. Kim, V. Wilke, et al., "Stabilizing Pure Water-Fed Anion Exchange Membrane Water Electrolyzers Through Membrane-Electrode Interface Engineering," *ACS Applied Materials & Interfaces* 16, no. 36 (2024): 47387–47395.
- 2. M. C. Yasin, M. Johar, A. Gupta, and S. Shahgaldi, "A Comprehensive Review of the Material Innovations and Corrosion Mitigation Strategies for PEMWE Bipolar Plates," *International Journal of Hydrogen Energy* 88 (2024): 726–747.
- 3. J. M. Conley, C. S. Lambright, N. Evans, et al., "Developmental Toxicity of Nafion Byproduct 2 (NBP2) in the Sprague-Dawley Rat With Comparisons to Hexafluoropropylene Oxide-Dimer Acid (HFPO-DA or GenX) and Perfluorooctane Sulfonate (PFOS)," *Environment International* 160 (2022): 107056.
- 4. W. Gui, H. Guo, X. Chen, et al., "Emerging Polyfluorinated Compound Nafion By-Product 2 Disturbs Intestinal Homeostasis in Zebrafish (*Danio rerio*)," *Ecotoxicology and Environmental Safety* 249 (2023): 114368.
- 5. C. C. Weber, J. A. Wrubel, L. Gubler, G. Bender, S. De Angelis, and F. N. Büchi, "How the Porous Transport Layer Interface Affects Catalyst Utilization and Performance in Polymer Electrolyte Water Electrolysis," *ACS Applied Materials & Interfaces* 15, no. 29 (2023): 34750–34763.
- 6. S. De Angelis, T. Schuler, M. A. Charalambous, F. Marone, T. J. Schmidt, and F. N. Büchi, "Unraveling Two-Phase Transport in Porous Transport Layer Materials for Polymer Electrolyte Water Electrolysis," *Journal of Materials Chemistry A* 9, no. 38 (2021): 22102–22113.

- 7. C. C. Weber, T. Schuler, R. De Bruycker, L. Gubler, F. N. Büchi, and S. De Angelis, "On the Role of Porous Transport Layer Thickness in Polymer Electrolyte Water Electrolysis," *Journal of Power Sources Advances* 15 (2022): 100095.
- 8. J. Kink, M. Ise, B. Bensmann, and R. Hanke-Rauschenbach, "Modeling Mechanical Behavior of Membranes in Proton Exchange Membrane Water Electrolyzers—IOPscience," 2023, accessed August 9, 2024, https://iopscience.iop.org/article/10.1149/1945-7111/acd47f/meta.
- 9. T. Lee and C. Yang, "A Parametric Study on the Deformation of Gas Diffusion Layer in PEM Fuel Cell," *Journal of Mechanical Science and Technology* 34, no. 1 (2020): 259–268.
- 10. Y. Tang, A. Kusoglu, A. M. Karlsson, M. H. Santare, S. Cleghorn, and W. B. Johnson, "Mechanical Properties of a Reinforced Composite Polymer Electrolyte Membrane and Its Simulated Performance in PEM Fuel Cells," *Journal of Power Sources* 175, no. 2 (2008): 817–825.
- 11. C. Liu, J. A. Wrubel, E. Padgett, and G. Bender, "Impacts of PTL Coating Gaps on Cell Performance for PEM Water Electrolyzer," *Applied Energy* 356 (2024): 122274.
- 12. T. Schuler, T. J. Schmidt, and F. N. Büchi, "Polymer Electrolyte Water Electrolysis: Correlating Performance and Porous Transport Layer Structure: Part II. Electrochemical Performance Analysis," *Journal of the Electrochemical Society* 166, no. 10 (2019): F555–F565.
- 13. J. E. Park, S. Y. Kang, S.-H. Oh, et al., "High-Performance Anion-Exchange Membrane Water Electrolysis," *Electrochimica Acta* 295 (2019): 99–106.
- 14. F. Rocha, R. Delmelle, C. Georgiadis, and J. Proost, "Effect of Pore Size and Electrolyte Flow Rate on the Bubble Removal Efficiency of 3D Pure Ni Foam Electrodes During Alkaline Water Electrolysis," *Journal of Environmental Chemical Engineering* 10, no. 3 (2022): 107648.
- 15. F. Rocha, R. Delmelle, C. Georgiadis, and J. Proost, "Electrochemical Performance Enhancement of 3D Printed Electrodes Tailored for Enhanced Gas Evacuation During Alkaline Water Electrolysis," *Advanced Energy Materials* 13, no. 1 (2023): 2203087.
- 16. F. Rocha, C. Georgiadis, K. Van Droogenbroek, et al., "Proton Exchange Membrane-Like Alkaline Water Electrolysis Using Flow-Engineered Three-Dimensional Electrodes," *Nature Communications* 15, no. 7444 (2024).
- 17. J. E. Park, H. J. Choi, S. Y. Kang, et al., "Effect of Pore Structures in Nickel-Based Porous Transport Layers for High-Performance and Durable Anion-Exchange Membrane Water Electrolysis," *International Journal of Energy Research* 46, no. 12 (2022): 16670–16678.
- 18. B. Chen, P. Mardle, and S. Holdcroft, "Probing the Effect of Ionomer Swelling on the Stability of Anion Exchange Membrane Water Electrolyzers," *Journal of Power Sources* 550 (2022): 232134.
- 19. F. Razmjooei, A. Farooqui, R. Reissner, A. S. Gago, S. A. Ansar, and K. A. Friedrich, "Elucidating the Performance Limitations of Alkaline Electrolyte Membrane Electrolysis: Dominance of Anion Concentration in Membrane Electrode Assembly," *ChemElectroChem* 7, no. 19 (2020): 3951–3960.
- 20. F. Razmjooei, T. Morawietz, E. Taghizadeh, et al., "Increasing the Performance of an Anion-Exchange Membrane Electrolyzer Operating in Pure Water With a Nickel-Based Microporous Layer," *Joule* 5, no. 7 (2021): 1776–1799.
- 21. L. Wang, T. Weissbach, R. Reissner, et al., "High Performance Anion Exchange Membrane Electrolysis Using Plasma-Sprayed, Non-Precious-Metal Electrodes," *ACS Applied Energy Materials* 2, no. 11 (2019): 7903–7912.
- 22. T. Schuler, J. M. Ciccone, B. Krentscher, et al., "Hierarchically Structured Porous Transport Layers for Polymer Electrolyte Water Electrolysis," *Advanced Energy Materials* 10, no. 2 (2020): 1903216.
- 23. T. Schuler, C. C. Weber, J. A. Wrubel, et al., "Ultrathin Microporous Transport Layers: Implications for Low Catalyst Loadings, Thin

- Membranes, and High Current Density Operation for Proton Exchange Membrane Electrolysis," *Advanced Energy Materials* 14, no. 7 (2024): 2307786
- 24. E. Borgardt, L. Giesenberg, M. Reska, et al., "Impact of Clamping Pressure and Stress Relaxation on The Performance of Different Polymer Electrolyte Membrane Water Electrolysis Cell Designs," *International Journal of Hydrogen Energy* 44, no. 42 (2019): 23556–23567.
- 25. F. N. Khatib, T. Wilberforce, O. Ijaodola, et al., "Material Degradation of Components in Polymer Electrolyte Membrane (PEM) Electrolytic Cell and Mitigation Mechanisms: A Review," *Renewable and Sustainable Energy Reviews* 111 (2019): 1–14.
- 26. Z. Bao, Y. Li, X. Zhou, F. Gao, Q. Du, and K. Jiao, "Transport Properties of Gas Diffusion Layer of Proton Exchange Membrane Fuel Cells: Effects of Compression," *International Journal of Heat and Mass Transfer* 178 (2021): 121608.
- 27. G. Chen, Q. Xu, J. Xuan, et al., "Numerical Study of Inhomogeneous Deformation of Gas Diffusion Layers on Proton Exchange Membrane Fuel Cells Performance," *Journal of Energy Storage* 44 (2021): 103486.
- 28. P. Irmscher, D. Qui, H. Janßen, W. Lehnert, and D. Stolten, "Impact of Gas Diffusion Layer Mechanics on PEM Fuel Cell Performance," *International Journal of Hydrogen Energy* 44, no. 41 (2019): 23406–23415.
- 29. M. Sauermoser, N. Kizilova, B. G. Pollet, and S. Kjelstrup, "Flow Field Patterns for Proton Exchange Membrane Fuel Cells," *Frontiers in Energy Research* 8 (2020): 482555.
- 30. W. Dong-Hui, Y. Lin-Zhi, P. Zhong-Yu, L. Cong-Da, L. Gang, and L. Qiao-Hui, "A Novel Intersectant Flow Field of Metal Bipolar Plate For Proton Exchange Membrane Fuel Cell: Design of New Intersectant Flow Field for PEMFC," *International Journal of Energy Research* 41, no. 14 (2017): 2184–2193.
- 31. J. H. Harmening, H. Devananthan, F.-J. Peitzmann, and B. O. el Moctar, "Aerodynamic Effects of Knitted Wire Meshes: CFD Simulations of the Flow Field and Influence on the Flow Separation of a Backward-Facing Ramp," *Fluids* 7, no. 12 (2022): 370.
- 32. B. Hasa, U. R. Aryal, S. Higashi, et al., "Porous Transport Layer Influence on Overpotentials in PEM Water Electrolysis at Low Anode Catalyst Loadings," *Applied Catalysis B: Environment and Energy* 361 (2025): 124616.
- 33. S. Stiber, H. Balzer, A. Wierhake, et al., "Porous Transport Layers for Proton Exchange Membrane Electrolysis Under Extreme Conditions of Current Density, Temperature, and Pressure," *Advanced Energy Materials* 11, no. 33 (2021): 2100630.
- 34. S. Campagna Zignani, M. L. Faro, A. Carbone, et al., "Performance and Stability of a Critical Raw Materials-Free Anion Exchange Membrane Electrolysis Cell," *Electrochimica Acta* 413 (2022): 140078.
- 35. M. Ranz, B. Grabner, B. Schweighofer, H. Wegleiter, and A. Trattner, "Dynamics of Anion Exchange Membrane Electrolysis: Unravelling Loss Mechanisms With Electrochemical Impedance Spectroscopy, Reference Electrodes and Distribution of Relaxation Times," *Journal of Power Sources* 605 (2024): 234455.
- 36. Z. Liu, S. D. Sajjad, Y. Gao, H. Yang, J. J. Kaczur, and R. I. Masel, "The Effect of Membrane on an Alkaline Water Electrolyzer," *International Journal of Hydrogen Energy* 42, no. 50 (2017): 29661–29665.
- 37. I. Gatto, A. Caprì, C. Lo Vecchio, S. Zignani, A. Patti, and V. Baglio, "Optimal Operating Conditions Evaluation of an Anion-Exchange-Membrane Electrolyzer Based on FUMASEP FAA3-50 Membrane," *International Journal of Hydrogen Energy* 48, no. 32 (2023): 11914–11921.
- 38. L.-H. Zhang, B. Huang, T. Zhou, and S. Xu, "Enhancing Oxygen Transport Performance With Improved Serpentine Flow Field on the Anode Side of the PEMEC," *International Journal of Hydrogen Energy* 82 (2024): 881–891.
- 39. M. Sepe, G.-H. Jung, G.-S. Doo, et al., "Multiscale Modeling of Oxygen Evolution Through Generated Bilayer Porous Transport Layers

for PEMWE Performance Improvement," *Journal of the Electrochemical Society* 171, no. 5 (2024): 054501.

40. S. Hoseini Larimi, A. Ramiar, R. Shafaghat, and Q. Esmaili, "The Effect of Geometric Parameters of PTL on Oxygen Transport in PEM Electrolysis Cell," *Proceedings of the Institution of Mechanical Engineers, Part C: Journal of Mechanical Engineering Science* 235, no. 24 (2021): 7484–7495.

41. A. Horsthemke and J. J. Schröder, "The Wettability of Industrial Surfaces: Contact Angle Measurements and Thermodynamic Analysis," *Chemical Engineering and Processing: Process Intensification* 19, no. 5 (1985): 277–285.

Supporting Information

Additional supporting information can be found online in the Supporting Information section.